Proportional electro-hydraulic valves: from analogue to digital control

Published on International Journal of Mechatronics and Automation, 2014, vol. 4, no. 2, pp. 93-103.
doi: 10.1504/IJMA.2014.062336, Inderscience Publishers

Proportional electro-hydraulic valves: from analogue to digital control

Authors:
Enrico Canuto(1), Wilber Acuña-Bravo(1), Marco Agostani(2), Marco Bonadei (2)

Affiliation:
(1) Politecnico di Torino, Dipartimento di Automatica e Informatica
Corso Duca degli Abruzzi 24, 10129 Torino, Italy
enrico.canuto@polito.it
wilber.acaunabravo@polito.it
(2) Atos SpA, Via alla Piana 57, Sesto Calende, Italy
magostani@atos.com
mbonadei@atos.com

Abstract - Proportional electro-hydraulic valves are ubiquitous as flow actuators in hydraulic systems. Flow regulation is the result of the accurate positioning of a spool driven by a solenoid and a position sensor. The overall control consists of two hierarchical loops: the inner loop is the solenoid current regulator with a closed-loop bandwidth close to 1 kHz. A model-based digital regulator of this kind has been presented elsewhere. The outer loop is a position tracking control, in charge of an accurate positioning of the spool with respect to the valve openings. The paper addresses the outer loop and concentrates on the conversion of an existing industrial analogue controller into a digital one. The analogue controller is a nonlinear proportional, integrative and derivative controller including a second-order derivative, and is capable of recovering a dead-band hysteresis. The digital conversion provides the necessary position derivatives through a state predictor, in order to withstand the 5-kHz Nyquist limit of the power supplier. As such it departs from traditional conversions dating back to more than ten years ago. The digital control law is fed by the state predictions and repeats the analogue control law with some improvements, as shown by the reported experiments.

Key words - Electro-hydraulics, proportional valve, digital control, hierarchy, position control.

Published on International Journal of Mechatronics and Automation, 2014, vol. 4, no. 2, pp. 93-103.
doi: 10.1504/IJMA.2014.062336, Inderscience Publishers

1. Introduction

Proportional electro-hydraulic valves are ubiquitous as flow actuators in hydraulic systems, and since more than ten years digital electronics and control have been integrated with them according to [1], [2], [3], [4] and [5]. Main advantages are configurability, parameter tuning, diagnostic and monitoring capabilities [2]. This paper concerns the conversion from analogue to digital control. An advantage of digital controllers is that they can be developed and implemented as model-based controllers. Embedded Model Control (EMC, see [6], [7] and [8]) is a methodology to do this, since it embeds the design model in the control unit.

Recent literature on hydraulic servo systems is mainly concerned with hydraulic actuators as in [9], [10], [11], [12] and with manipulators [13]. Control design methodologies ranges from adaptive control [11], [12], [13], to nonlinear back-stepping [9] and to mixed sensitivity H-infinity design [14]. Control design is usually approached in continuous time. Here digital control is fully designed in discrete time, and we adopt the way of separating control law and state predictor. In the literature no state predictor is implemented for estimating the state variables of the control law, but a single output feedback is directly designed. Here the output feedback is separated into a state predictor as a first step toward a model-based control that includes active disturbance rejection as in the current regulator [15]. Disturbance rejection is still in charge of the integrative part of the PIDD^2 (proportional, integrative, derivative and double derivative) control law. Since the state predictor provides position, velocity and acceleration in a unified manner, the control law simplifies to a state feedback plus integrative dynamics.

A first step of the academic authors in the field of electro-hydraulic valves was made some years ago [16], [17]. Recently the research was resumed and experimental results of the solenoid current regulator have been reported in [15]. The paper extends modelling, control design and experiments to position control [18].

Flow regulation is the result of the accurate positioning of a shaped cylinder, the spool, which is driven by a solenoid and a position sensor, usually a LVDT (Linear Variable Differential Transformer). The solenoid force being unidirectional, unlike voice coil motors, requires a contrasting spring assembly for disposing of a differential force. Positioning accuracy is contrasted by solenoid plunger friction, by fluid forces depending on the pressure drop across the valve openings, by complexity and hysteresis of the electromagnetic force generated by the solenoid. Friction is alleviated by interposing a self-lubricating surface between plunger and magnetic core. The magnetic circuit is shaped to obtain an electromagnetic force which is close to be proportional to the driving current and constant in the operating region of the spool displacement. The magnetic circuit is made of soft ferromagnetic material, but a hysteresis cycle remains. The hysteresis width of the study case reaches 0.3 A, which is about 10% of the peak current. The cycle is travelled as in a dead band, and the bandwidth must be recovered in short times (< 2 ms) to avoid distortion of the reference position profile. The LVDT position sensor is mounted on the solenoid plunger. The spool is not rigidly connected to the plunger, but is kept in contact by a spring assembly. The solenoid circuit is driven by a current regulator and a 10-kHz PWM (Pulse Width Modulation) power amplifier.

The paper is organized as follows. A review of the plunger and spool dynamics is given in Section 2 together with the experimental profile of the hysteresis cycle. Hysteresis has been modelled from experimental data as a static dead band plus a first-order dynamics. The result is a nonlinear dynamics from current to the measured plunger position having relative degree equal to three. The dynamic model assumes a unique moving body made by plunger and spool, which relies on the assumption of ideal and steady contact between them [14], [19]. Section 3 firstly recalls requirements and performance of the current regulator [15]. The regulator plays the role of the inner loop of a hierarchical control, since the current reference is provided by the position control (the outer layer). The analogue position controller is briefly outlined, since the digital position control has been designed to repeat and improve analogue performance. The core of the analogue control is an industrial nonlinear PIDD^2 (proportional, integrative, derivative and double derivative), which aims to recover the hysteresis dead band. Digital conversion relies on a fourth-order state predictor that has been designed with the aid of the EMC methodology. The state predictor provides the variables entering the control law. Analysis and design of the state predictor is provided with the aid of some theorems and of the literature about Bode's theorem [20], [21]. The control law repeats the analogue PIDD^2, but employs a reshaped nonlinear function. Section 4 presents and discusses experimental results.

2. Dynamic model

2.1. Solenoid dynamics

Solenoid current dynamics and digital control have been presented in [15]. The current regulator is an inner loop of the overall valve control system enlarging the solenoid open-loop bandwidth. The closed-loop dynamics from

current reference $\underline{I}(t)$ to the measurement $I(t)$ has been designed and experimentally tested to approximate a 0.2 ms delay plus jitter. The following equations apply:

$$\begin{aligned} &I(t) = \underline{I}(t-\tau) + e_I(t) \\ &\left|e_I(t)\right| \le 1.5 \text{ mA},\ \tau = 0.2 \text{ ms},\ 0 \le \underline{I} \le I_{\max} = 3 \text{ A} \end{aligned} . \quad (1)$$

2.2. Plunger and spool dynamics

Assuming rigid connection between plunger and spool, the following state equations can be written

$$\begin{aligned} &\dot{x} = v,\ x(0) = x_0 \\ &m\dot{v} = F_s(x,a,I,\dot{I}) - F_a(x,z,\dot{z},v) - F_f(x,v,\Delta p) - \\ &-K(X_0 + x),\ v(0) = v_0 \\ &\dot{z} = g(z,v),\ \ z(0) = z_0 \end{aligned} . \quad (2)$$

They are valid within the spool stroke region, i.e. between the rest position $X_{\min}$ imposed by the spring assembly and the end stroke $X_{\max}$, the latter fixing a limit to operations:

$$\begin{aligned} &X_{\min} \le x \le X_{\max} \\ &X_{\min} \cong -2.5 \text{ mm},\ X_{\max} \cong 1.25 \text{ mm} \end{aligned} . \quad (3)$$

The notations of (2) are as follows.

1) x and v denote spool displacement and velocity from the sensor zero. The sensor zero is close to the spool hydraulic zero. $m \cong 0.1$ kg is the total moving mass of the plunger and spool. The mass-spring frequency $f_o = (2\pi)^{-1}\sqrt{K/m} \cong 50$ Hz can be taken as the open-loop bandwidth.
2) $F_f(x,v,\Delta p)$ denotes fluid visco-elastic forces satisfying $F_f(0,0,\Delta p) = 0$ and $F_f(x,0,0) = 0$.
3) $F_a(x,z,\dot{z},v)$ is the friction force, depending on the LuGre deformation z and rate $\dot{z}$ [22]. At zero position and deformation rate it satisfies

$$F_a(0,z,0,v) = \operatorname{sgn}(v) F_{a0} . \quad (4)$$

4) $F_s(x,I,\dot{I}),\ 0 \le I \le I_{\max}$ is the electromagnetic force including magnetic hysteresis. At zero position, it is balanced by the return spring pre-load KX_0 and by the static friction F_{a0} in (4) as follows:

$$F_s(0,I_0,\operatorname{sgn}(\dot{I})) = KX_0 - \operatorname{sgn}(v) F_{a0} . \quad (5)$$

5) Because of $\operatorname{sgn}(\dot{I})$ (magnetic hysteresis) and of $\operatorname{sgn}(v)$ (friction), the bias current I_0 in (5) is not uniquely defined, but it may vary in the order of fractions of Amperes. The experimental magnetic hysteresis cycle is in Figure 1. Increasing current and force occurs on the right edge of the cycle.

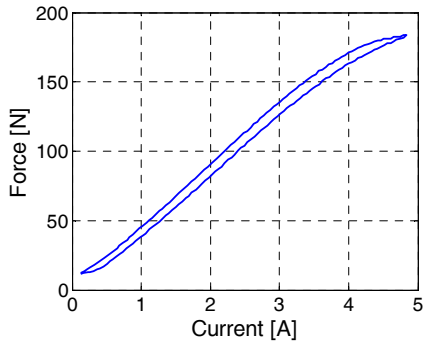

Figure 1 Experimental hysteresis cycle.

The hysteresis cycle is clearly of magnetic origin since the force depending on the magnetic flux lags behind the solenoid current. Instead of using standard models of magnetic hysteresis like Jiles-Atherton and Preisach [23], we preferred fitting a dynamical model to experimental data, taking into account that the magnetic circuit properties are steady and only depend on temperature. Further studies and experiments pointed out that the hysteresis cycle in Figure 1 is of dead-band type. In other terms, when the current derivative changes sign, the output force remains pretty constant waiting for the current to reach the decreasing edge (the left edge in Figure 1). Nonlinearities of this kind have been widely studied (see for instance [24] and [25]). The dead-band type is confirmed by the frequency responses (only the argument is shown) in Figure 2. The sinusoidal response of a regular and normalized dead-band cycle (both edges are parallel lines having unit slope) shows uniform attenuation and angular phase, whichever be the input frequency. Attenuation and phase depends on the input magnitude. Figure 2 shows uniform phase (about 20 to 30 degrees) with respect to a first-order (plus delay) harmonic response fitting experimental data. The fitting delay corresponds to a PWM cycle (0.1 ms) and can be neglected by control design. The first-order time constant $\tau_a = 1 \div 2$ ms cannot be neglected in view of a target closed-loop delay of the order of $\tau_c = 3$ ms. Thus $F_s(\cdot)$ has been modelled as

$$\begin{aligned} &\dot{c}(t) = \left(-c(t) + b_s(I,\dot{I})\right)/\tau_a,\ c(0) = c_0 \\ &F_s(t) = \underline{F}_s(x,c) \end{aligned} \quad (6)$$

where $b_s(\cdot)$ is the dead-band function, c is a current [A], and $\underline{F}_s(\cdot)$ is the average electromagnetic force.

Figure 2 Current-to-force frequency response (argument).

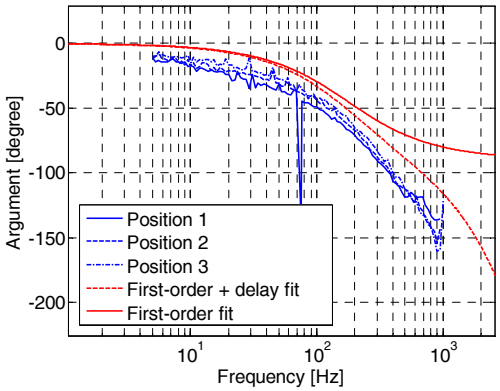

2.3. Position sensor

The LVDT sensor is sinusoidally excited with a frequency f_s close to the PWM Nyquist frequency $f_{\max} = 5$ kHz and has a bandwidth (BW) $\varphi_s = 500$ Hz. Figure 3 shows the unilateral root spectral density (briefly PSD) of the measurement zero-mean error. Data were retrieved upstairs (wide-band noise) and downstairs (digitally filtered noise) a digital anti-aliasing filter. The low-frequency content is respected until 1 kHz, just above the sensor BW, and well beyond the target position BW of about 100 Hz.

Figure 3 Spectral density of the position sensor noise.

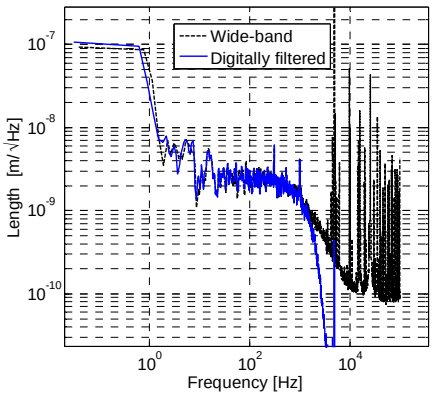

The sensor dynamic model is the following

$$\begin{aligned} \dot{x}_s(t) &= \left(-x_s(t) + K_s\left(1+\partial K_s\right)x(t) + e_s(t)\right)/\tau_s \\ y_s(t) &= x_s(t) + b_s,\ V_m(t) = \mathrm{sat}\left(y_s, V_{m,\max}\right) \\ e_s(t) &= \sum_{k=1}^{\infty} E_{sk}\sin\left(2\pi k f_s t + \varphi_{sk}\right) + \eta_s \end{aligned} \quad . \quad (7)$$

In (7) x_s is the state of output low-pass filter, K_s is the sensor gain with scale factor uncertainty ∂K_s, the zero-mean input noise e_s is the sum of a random error η_s and of a periodic component tuned on the excitation frequency f_s (the resonance peaks in Figure 3). The input noise is partially filtered by the output low-pass filter in (7) as shown in Figure 3 (wide-band noise). The basement of the higher frequency content does not decay due to a mix of numerical errors and residual aliasing, notwithstanding a 200 kHz sampling. The bias b_s only accounts for electronics and sensor mounting errors, and can be identified and corrected, unless for thermal variations. The ultimate bias is the offset between the spool hydraulic zero and the sensor zero. The function $\mathrm{sat}\left(y, y_{\max}\right)$ stands for $|y| \le y_{\max}$.

3. Analogue and digital control

3.1. Requirements

Position requirements are similar to current requirements. Some metrics for experimental evaluation of the position control for hydraulic systems are reported in [26]. They include mean and absolute positioning accuracy, corresponding to the root mean square (RMS) error and to the maximum absolute error, respectively. Both errors are adopted. No transient metrics seems suggested in [26], unlike here where delay and slew rate are evaluated. Given a reference position signal $r(t)$, the plunger position x (the same as the spool position under rigidity assumption) is delayed and corrupted as follows

$$\begin{aligned} x(t) &= r\left(t - \tau\left(r_{\max}\right)\right) + \eta_x(t) \\ \tau_x\left(r_{\max}\right) &\le 5 \text{ ms},\ |\eta_x(t)| \le 10\ \mu\text{m} \end{aligned}, \quad (8)$$

where η_x is the residual tracking error which is defined as the difference between the total tracking error $e_x = r - x$ and the nominal tracking error $\underline{e}_x$. The latter is imposed by the target delay τ_x and by the reference rate $\dot{r}_x$ as follows

$$\eta_x(t) = e_x(t) - \underline{e}_x(t),\ \underline{e}_x(t) = \dot{r}_x(t)\tau_x. \quad (9)$$

The maximum delay refers to the maximum stroke $2X_{\max}$ in (3) (100%), but becomes smaller for intermediate and small strokes, in which cases it reaches 3 ms. The slew rate must be of the order of 0.25 m/s to repeat a full-stroke 50 Hz ramp.

3.2. The analogue position loop

The analogue position loop is a proportional (P) plus derivative (D), plus double derivative (D^2) action. It is completed with a feedforward and integrative (I) action and a dead-band compensation. The double derivative is mandatory to raise the loop phase delay to about -135 degrees in the frequency band above the open-loop bandwidth of $f_o \cong 50$ Hz. In this way the closed-loop BW f_c can be widened up to 100 Hz. The latter frequency stays in the range $80 \div 150$ Hz of the cut-off frequency of the current-to-force dynamics in (6) and is sufficiently lower than the current regulator BW in (1).
The state equations of the nonlinear $PIDD^2$ controller in Figure 4 are the following ones.

Published on International Journal of Mechatronics and Automation, 2014, vol. 4, no. 2, pp. 93-103.
doi: 10.1504/IJMA.2014.062336, Inderscience Publishers

$$\begin{bmatrix}\dot{x}_i\\ \dot{x}_d\\ \dot{x}_{d1}\\ \dot{x}_{d2}\\ \dot{x}_m\end{bmatrix}(t)=\begin{bmatrix}0 & 0 & 0 & 0 & -1/\tau_i\\ 0 & -1/\tau_d & 0 & 0 & -1/\tau_d\\ 0 & 1/\tau_{d1} & -1/\tau_{d1} & 0 & 0\\ 0 & \dfrac{\tau_{z1}}{\tau_{d1}\tau_{d2}} & -\dfrac{\tau_{z1}}{\tau_{d1}\tau_{d2}} & -1/\tau_{d2} & 0\\ 0 & 0 & 0 & 0 & -1/\tau_m\end{bmatrix}\begin{bmatrix}x_i\\ x_d\\ x_{d1}\\ x_{d2}\\ x_m\end{bmatrix}(t)+\begin{bmatrix}1/\tau_i & 0\\ 0 & 0\\ 0 & 0\\ 0 & 0\\ K_m/\tau_m & 0\end{bmatrix}\begin{bmatrix}V_r\\ V_m\end{bmatrix}(t),\quad \begin{bmatrix}x_i\\ x_d\\ x_{d1}\\ x_{d2}\\ x_m\end{bmatrix}(0)=0$$

$$y_c(t)=\begin{bmatrix}K_i & K_d\dfrac{\tau_{z1}\tau_{z2}}{\tau_{d1}\tau_{d2}} & -K_d\dfrac{\tau_{z1}\tau_{z2}}{\tau_{d1}\tau_{d2}} & K_d\left(1-\dfrac{\tau_{z2}}{\tau_{d2}}\right) & 0\end{bmatrix}\begin{bmatrix}x_i\\ x_{d1}\\ x_{d2}\\ x_{d3}\\ x_m\end{bmatrix}(t)+\begin{bmatrix}K_r & 0\end{bmatrix}\begin{bmatrix}V_r\\ V_m\end{bmatrix}(t)+K_p(V_r-V_m)\quad . \tag{10}$$

$$\Delta V_c(t)=\mathrm{sat}(y_c),|V_r|\le V_{r,\max},|\Delta V_c|\le \Delta V_{c,\max}$$

Figure 4 Block-diagram of the analogue position controller.

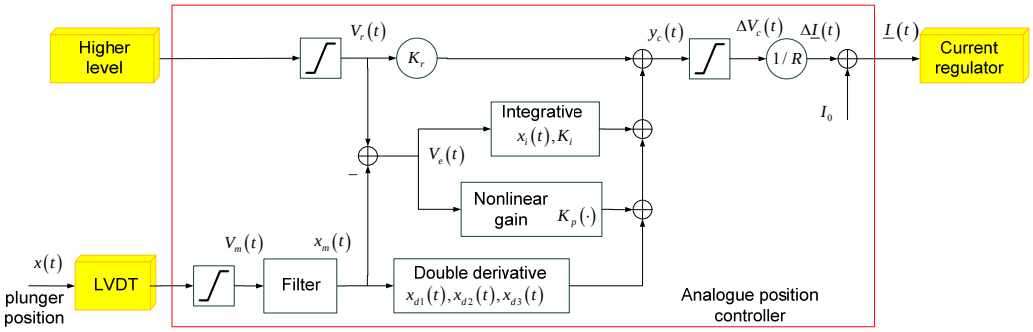

The variable x_i is the integrative state, the triple x_d, x_{d1} and x_{d2} is the derivative state vector, x_m is the state of the measurement low-pass filter. The reference and sensor voltages are V_r and V_m. The nonlinear function $K_p(\cdot)$, replacing the proportional gain, is shown in Figure 5. In the analogue control circuit, it is implemented as a piecewise curve, whereas in the digital version a smooth function has been implemented. Units in Figure 5 are the voltage units of the analogue operational amplifiers that saturate to about 13 V.

Figure 5 Nonlinear position error function in voltage units.

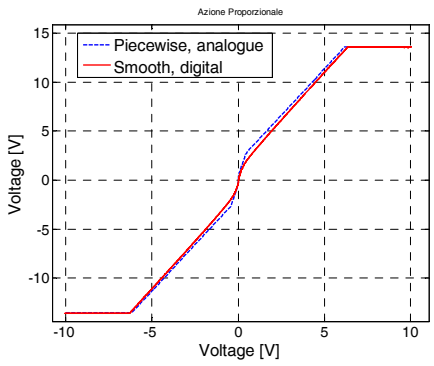

The reference current to the analogue current regulator is computed as

$$\underline{I}(t)=\frac{\Delta V_c(t)}{R}+I_0 \tag{11}$$

Typical parameters are in Table 1.

Table 1 Main analogue controller parameters

Parameter	Symbol	Unit	Value
Feedforward gain	K_r	V/V	0.3

Differential gain	k_p	V/V	4~40
Integrative gain	K_i	V/V	0.4~0.6
Derivative gain	K_d	V/V	4
Solenoid resistance	R	Ω	4

The nonlinear monotonic function $K_p(\cdot)$ in (10) can be approximated around each error point V_{e0} of $V_e = V_r - V_m$ as follows

$$K_p(V_{e0} + \Delta V_e) = \\ = \Delta V_{c0}(V_{e0}) + k_P(V_{e0})\Delta V_e + \delta V_c(V_{e0}, \Delta V_e), \quad (12)$$

where ΔV_e is the differential error, k_p the differential gain in Table 1, ΔV_{c0} the error offset, and δV_c is the approximation error. In the analogue case, due to piecewise implementation, the approximation error δV_c is first order in ΔV_e which causes jumps in the reference current. The smooth implementation of the digital control shown in Figure 5 aims to avoid them.

Figure 6 Magnitude of the feedback bode plot of the analogue and digital controllers.

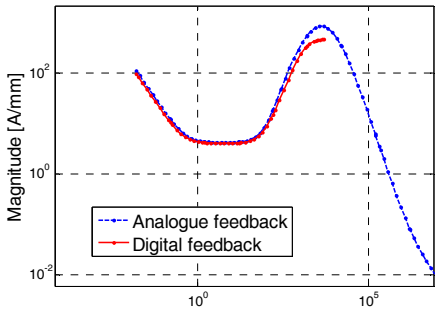

The feedback transfer function $K(s)$ of the analogue controller, that can be computed from (10), and that of digital controller are compared in Figure 6. The digital control plot halts at the PWM Nyquist frequency $f_{\max} = 5$ kHz. The higher-frequency roll-off of the analogue feedback at $f > f_{\max}$ is a consequence of the double derivative action. Since a similar decay cannot be implemented in the discrete-case, because of the PWM Nyquist frequency, it has been surrogated as follows.

1) Suitable (analogue/digital) filters have been designed to avoid aliasing as shown in Figure 3 for the position sensor errors.
2) Derivative and double derivative are surrogated by a fourth-order state predictor which is driven by the position measurement, as explained in Section 3.3.
3) Close to $f_{\max}$, the magnitude of the digital $K(s)$ has been attenuated as it can rely on the wider band of the current regulator in (1).

3.3. Digital control: state predictor

The block-diagram of the hierarchical digital control is in Figure 7. The core of the control unit is the state predictor that computes the position derivatives.

Only the digital measured position $\tilde{y}_x$ enters the state predictor, which corresponds to assume that the overall plunger and spool acceleration $a(i)$ (in length units [m]) is completely unknown. The assumption imposes to model the unknown $a(i)$ as a stochastic process which is sum of a drift d and of a white noise w_a, in agreement with the EMC methodology ([6], [7] and [8]). Since no statistical model is attached to d and w_a, and no Kalman filter is employed, w_a can be better interpreted as an arbitrary and bounded signal, but having zero mean. It could be referred as an uncertainty input, but the term 'noise' is 'used' for short. The drift is driven by the noise w_d. The driving noise vector

$$\mathbf{w}^T = \begin{bmatrix} w_a & w_d \end{bmatrix}, \quad (13)$$

is estimated from the model error e_m, which is defined by the difference between the anti-aliased measurement y_x and the predicted position x as follows

$$e_m(i) = y_x(i) - x(i) = y_x(i) - y_m(i). \quad (14)$$

Figure 7 Block-diagram of the digital control.

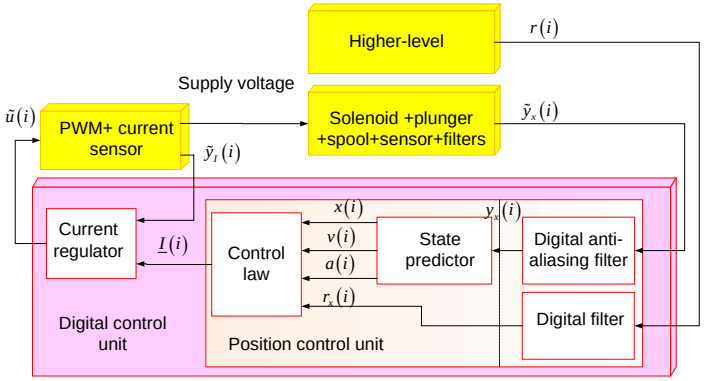

Published on International Journal of Mechatronics and Automation, 2014, vol. 4, no. 2, pp. 93-103.
doi: 10.1504/IJMA.2014.062336, Inderscience Publishers

Since no noise component exists between the acceleration a and the position x, only a dynamic feedback can connect the model error e_m and the noise vector $\mathbf{w}$ in a stabilizable way (see [7]). The resulting state equation is found to be:

$$\begin{aligned}&\mathbf{x}(i+1)=A\mathbf{x}(i)+Ly_x(i),\ \mathbf{x}(0)=\mathbf{x}_0\\&\mathbf{y}(i)=C_m\mathbf{x}(i)+D_m y_x(i)\end{aligned}. \quad (15)$$

The three matrices, the state vector $\mathbf{x}$ and the output vector $\mathbf{y}$ in (15) hold

$$\begin{aligned}&\mathbf{x}=\begin{bmatrix}x\\v\\d\\q\end{bmatrix},\ A=\begin{bmatrix}1&1&0&0\\-l_a&1&1&m_a\\-l_d&0&1&m_d\\-1&0&0&1-\beta\end{bmatrix},\ L=\begin{bmatrix}0\\l_a\\l_d\\1\end{bmatrix}\\&\mathbf{y}=\begin{bmatrix}y_m=x\\v\\a\end{bmatrix},\ C_m=\begin{bmatrix}1&0&0&0\\0&1&0&0\\-l_a&0&1&m_a\end{bmatrix},D_m=\begin{bmatrix}0\\0\\l_a\end{bmatrix}\end{aligned}. \quad (16)$$

The five unknown gains in (16) are $l_a, l_d, m_a, m_d, \beta$. The state q is the feedback state, v is the position increment [m] and a is the DT acceleration [m]. The state predictor contains a dynamic feedback and a two-column gain vector, what becomes clear by expressing the noise vector estimate

$$\mathbf{w}(i)=\begin{bmatrix}w_a\\w_d\end{bmatrix}(i)=\begin{bmatrix}l_a&m_a\\l_d&m_d\end{bmatrix}\begin{bmatrix}y_x-y_m\\q\end{bmatrix}. \quad (17)$$

3.4. Digital control: state predictor design

The gains in (16) are designed by fixing the four closed-loop eigenvalues $\Lambda_m=\{\lambda_1=1-\gamma_1,...,\lambda_4=1-\gamma_4\}$ of the state predictor. Employing the complementary eigenvalues $\gamma_k=1,...,4$ and setting $\gamma=\lambda-1$ allows the characteristic polynomial $P_A(\lambda)$ of A in the form

$$\begin{aligned}&P_A(\lambda)=\prod_{k=1}^4(\lambda-\lambda_k)=\prod_{k=1}^4(\gamma+\gamma_k)=\\&=\gamma^4+c_3\gamma^3+c_2\gamma^2+c_1\gamma+c_0=\\&=\gamma^4+\beta\gamma^3+l_a\gamma^2+(m_a+l_d+\beta l_a)\gamma+m_d+l_d\beta\end{aligned}, \quad (18)$$

where the assumption $0<\gamma_k\le 1$ implies $c_k>0$. Equality of known and unknown coefficient in (18) yields four nonlinear gain equations

$$\begin{aligned}&\beta=c_3,\ l_a=c_2,\ m_a+l_d+\beta l_a=c_1\\&m_d+l_d\beta=c_0\end{aligned}, \quad (19)$$

which admit infinite solutions because of five unknowns. Further since $\gamma_k<\sum_i^4\gamma_i$, it holds

$$\begin{aligned}&c_1-\beta l_a=c_1-c_3c_2=\\&=\sum_{i\ne j\ne k}^4\gamma_i\gamma_j\gamma_k-\sum_i^4\gamma_i\sum_{i\ne j}^4\gamma_i\gamma_j<0\end{aligned}. \quad (20)$$

The set of solutions is built by rewriting the last two equations of (19) as functions of the parameter $l_d\in\mathscr{C}$:

$$\begin{aligned}&m_a=c_1-\beta l_a-l_d,\ m_d/\beta=c_0/\beta-l_d\\&\mathscr{C}=\{l_d;-l_{\min}=c_1-\beta l_a\le l_d\le c_0/\beta=l_{\max}\}.\\&l_{\min}>0, l_{\max}>0\end{aligned} \quad (21)$$

The next theorem states the invariance of transfer function within the convex set $\mathscr{C}$, which implies that l_d may be arbitrarily selected.

Theorem 1. The following transfer functions of the state predictor (16), namely

$$V_{px}(z)=\frac{x(z)}{y_x(z)},\ V_{pv}(z)=\frac{v(z)}{y_x(z)},\ V_{pa}(z)=\frac{a(z)}{y_x(z)}, \quad (22)$$

are invariant for $l_d\in\mathscr{C}$.

Proof. Using the notation $s=z-1$, the transfer functions in (22) are easily obtained as

$$\begin{aligned}&V_{px}(s=z-1)=\frac{c_2s^2+c_1s+c_0}{s^4+c_3s^3+c_2s^2+c_1s+c_0}\\&V_{pv}(s=z-1)=sV_{px}(s=z-1)\\&V_{pa}(s=z-1)=s^2V_{px}(s=z-1)\end{aligned}. \quad (23)$$

Since they only depend on the coefficients c_k, $k=0,...,3$ in (18), they are independent of the particular solution of (19). Thus the simplest solution is to assume $l_d=0$. □

The second design issue is to select the four complementary eigenvalues γ_k in (20). The requirements refer to the complementary sensitivity $V_p(z)$ in (23). They fix an upper bound $V_{p,\max}$ to the overshoot and a lower bound $f_{v,\min}$ to the bandwidth $f_v<f_{\max}$ as follows

$$\begin{aligned}&\max_{|f|<f_{\max}}\left|V_p\left(e^{j2\pi fT}\right)\right|\le V_{p,\max}=1.25\\&\max_{|f|\ge f_v}\left|V_p\left(e^{j2\pi fT}\right)\right|\le\alpha=0.1\end{aligned}. \quad (24)$$

According to [20], Corollary 2, the Poisson's integral formula allows to write the integral equality

$$\ln|K_\infty|=\int_0^{f_{\max}}\ln\left|V_p\left(e^{j2\pi fT}\right)\right|df/f_{\max} \quad (25)$$

under the assumption that $V_p(z)$ is Hurwitz and minimum-phase. The gain K_∞ is obtained by expanding $V_p(z)$ in (23) around $z-1\to\infty$ and by taking the lowest-order term, which yields

$$V_{p\infty}(z)=\lim_{z\to\infty}V_p(z-1)=K_\infty(z-1)^{-2},\ K_\infty=c_2. \quad (26)$$

Further, if $f<f_{\max}$, (26) can be approximated by making explicit the bandwidth f_v, what in turn provides the expression of K_∞ as follows

$$\left|V_{p\infty}\left(e^{j2\pi fT}\right)\right| \cong \left(\frac{2\pi f_v T}{2\pi fT}\right)^2 = \left(\frac{f_v}{f}\right)^2 . \qquad (27)$$
$$K_\infty \cong \left(\pi f_v / f_{\max}\right)^2$$

According to [21], the integral in (25), and therefore $|K_\infty|$, can be upper bounded using the bounds in (24) in the following manner:

$$\ln|K_\infty| \cong 2\ln\pi + 2\ln\left(f_v / f_{\max}\right) \le \qquad (28)$$
$$\le \ln V_{p,\max}\left(f_v / f_{\max}\right) + \ln\alpha\left(1 - f_v / f_{\max}\right)$$

Given $V_{p,\max}$ and α, (28) can be solved in terms of the frequency ratio $\phi = f_v / f_{\max}$, what provides a lower bound to f_v. Figure 8 shows the ratio $\rho(\varphi)$ obtained by rearranging (28) as follows

$$\rho(\varphi) = \frac{2\ln\varphi - \left(\ln V_{p,\max} - \ln\alpha\right)\varphi}{\ln\alpha - 2\ln\pi} \le 1 . \qquad (29)$$

The candidate f_v is obtained for $\rho(\varphi) \le 1$. With the help of (26) and (27), Figure 8 yields

$$f_v \ge 0.25\, f_{\max}, \; c_2 \cong 0.6 . \qquad (30)$$

Figure 8 The function providing a lower bound to the complementary sensitivity bandwidth.

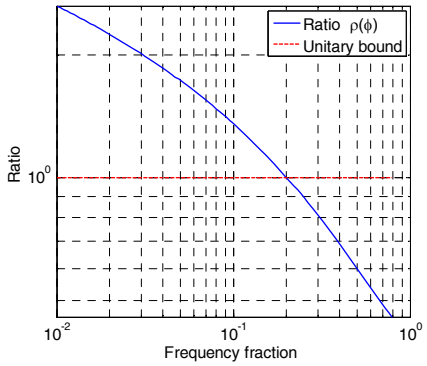

The complementary eigenvalues γ_k, $k = 1,\ldots,4$ in (20) have been selected to satisfy (30). Their values are listed in Table 2.

3.5. *Digital control: control law*

The output variables of (16) and the filtered reference $r_x(i)$ are the input variables of the digital control law that emulates the analogue controller as follows

$$\underline{I} = I_0 + b\left(K_{dr} r_x - K_{di} x_i - K_{da} a - K_{dv} v - \frac{K_{dp}(\cdot)}{K_s}\right)$$
$$x_i(i+1) = x_i(i) + e_x(i), \; x_i(0) = x_{i0} \qquad (31)$$
$$e_x(i) = r_x(i) - x(i), \; 0 \le \underline{I}(i) \le I_{\max}$$

The control law (31) includes the bias current I_0, the feedforward term proportional to r_x, the integrative action proportional to x_i, acceleration and rate feedback and the nonlinear feedback $K_{dp}(\cdot)$, which is function of the tracking error e_x in voltage units. The feedback gains and the function $K_{dp}(\cdot)$ have been properly tuned for emulating the analogue control response as in Figure 6. The main digital control parameters are in Table 2. The four feedback gains in (31) are proportional to the relevant analogue gains in Table 1.

The nonlinear function in Figure 5 has been designed to invert the nonlinearity (6) inside the open-loop band $f < f_o \cong 50$ Hz. The dead-band phase delay of about $20 \sim 30$ degrees (see Figure 2) corresponds to a time delay which is not negligible with respect to the target τ_x in (8). The abscissa corresponds to the tracking error e_x in (31). A sketch of the proof of $K_{dp}(\cdot)$ is the following. Within the open-loop BW f_o one may approximate (2) and (6) with the stationary and average equation

$$\phi c(t) \cong K x(t), \; \phi \cong 35 \text{ Vs/m} , \qquad (31)$$

where ϕ is the average flux linear density of the force profiles. Then, the tracking error e_x within the closed-loop bandwidth $f_c > f_o$, must equal the derivative of the reference signal r_x, which is required to bring the static error to zero. In other words the tracking error tends to be proportional to the plunger rate $\dot{x}$ and through (31) to the current derivative $\dot{c}(t)$. Therefore, inversion of the dead-band $b_s(I, \dot{I})$ in (6) may be obtained by approximating the inverse map

$$I(t) = b_s^{-1}(c, \dot{c}) . \qquad (32)$$

The higher proportional gain around the origin in Figure 5 does the purpose.

Table 2 Main digital control parameters

Parameter	Symbol	Unit	Value
Length to current gain	b	mm/A	0.035
Voltage to length gain	K_s	V/mm	3.3
State predictor eigenvalues	$\{\gamma_1,\ldots,\gamma_4\}$		2×0.4, 0.04,0.04

4. Experimental results

Experimental tests were performed on a test rig which consists of a pump, the valve under test and a second valve acting as a load. The supply pressure P_s and the tank oil temperature are measured.

4.1. *Time response*

Figure 9 50% square-wave reference and response.

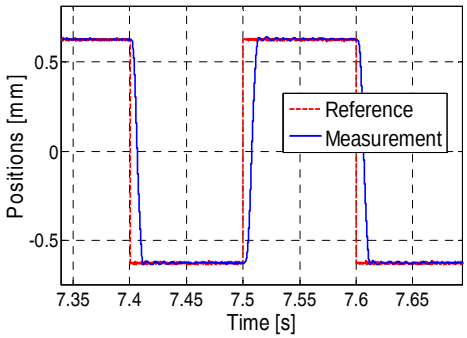

The results below refer to $P_s = 20$ bar. The time responses to square and triangular waves are shown in Figure 9 and Figure 10. Figure 9 refers to a square-wave reference. The response is delayed because of the current limit (accounted for by the position control (31)) and by the current regulator slew rate in (1). Figure 10 refers to a triangular wave. Figure 10 proves that the target delay between reference and response is close to 3 ms also for a 70% stroke reference.

Figure 10 70% triangular-wave response.

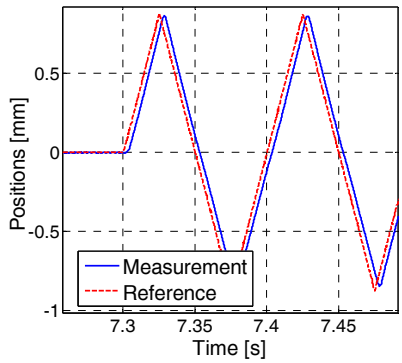

4.2. Frequency response

The frequency response to a small- and large-signal sinusoidal reference is shown in Figure 11 and Figure 12. Small signals correspond to the 5% of the maximum stroke. Large signals to the 90%. Figure 11 shows the Bode magnitude of the frequency response. A better regularity of the digital response than the analogue controller is evident. Rather significant is the constant unit response in the case of small signals from DC to 100 Hz, which emulates the target delay response.

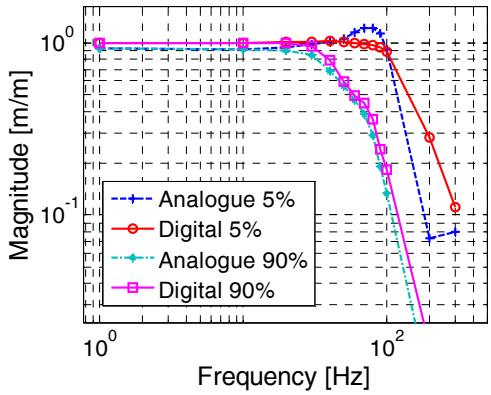

Figure 11 Closed-loop Bode magnitude at different strokes.

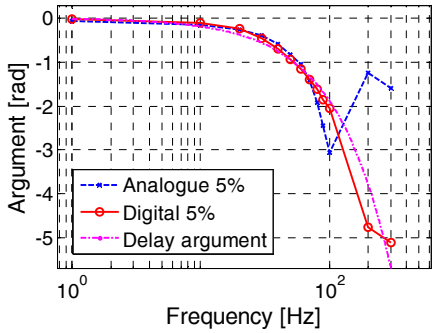

Figure 12 5% closed-loop Bode argument.

Figure 12 plots the argument of the small signal response and confirms the designed delay response (dash-dot profile) at least from DC to 100 Hz. After that, the digital argument becomes lower than the delay argument in agreement with the magnitude drop in Figure 11. The small-signal responses in Figure 11 and Figure 12 look very similar to the small-signal responses in [14].

4.3. Residual analysis

Figure 13 show the residual measured tracking error η_x, which was defined in (9) as the total tracking error e_x minus the nominal error $\underline{e}_x$. The residual tracking error is due to uncompensated disturbances and to the reference signal noise. Figure 13 shows that the residual error is pretty independent of the specific reference shape, thus being function of the non-rejected disturbance, mainly fluid forces. Of course it depends on the reference period P_r, which in this case amounts to 0.1 s ($f_r = 10$ Hz).

Figure 13 Residual (total less nominal) tracking error.

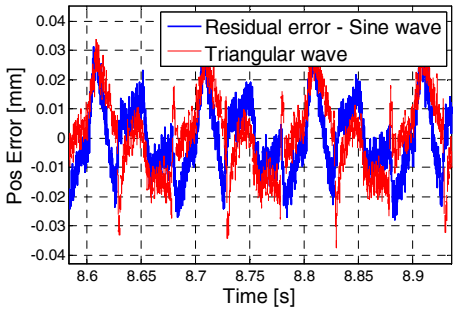

More information can be obtained from the PSD $S_e(f)$ of the residual error (not reported). The latter can be decomposed into three components. The flat basement is of the order of 0.04 μm/$\sqrt{\text{Hz}}$ and is due to the noise of the reference signal (the latter is provided by a higher level control). The basement value is of the same order of the flat mid frequency PSD of the measurement noise in Figure 3. A series of resonance peaks occur at the multiples of the reference frequency f_r. The on-going design effort is to further abate such components, whose magnitude mainly depends on the pressure drop level.
A summary of the requirements and of the preliminary performance is reported in Table 3.

Table 3 Requirements and performance summary

Parameter	Symbol	Unit	Value	Performance
Target delay	τ_x	ms	<5	3 ms @ 70 % triangular wave and 5% sine reference, acceptable
Residual tracking error	$\lvert\eta_x\rvert$	mm	0.01	<0.04 @ $P_s = 20$ bar , to be improved
Slew rate		m/s	0.25	0.12 @ 50% square wave reference, to be improved

5. Conclusion

The digital conversion of an industrial analogue controller driving a proportional valve has been outlined. The conversion method has been preceded by a short description of the valve dynamics, emphasizing a dynamic dead-band hysteresis between current and force. Dead-band compensation requires a nonlinear feedback and a PIDD^2 analogue controller. Derivatives are directly provided indiscrete-time through a state predictor which was developed according to the Embedded Model methodology. The design of the state predictor allows to tune the frequency response from the position measurement to the estimated position, velocity and acceleration. In this way the requirements, that in this case are expressed in terms of the overall feedback transfer function of the analogue PIDD^2, can be easily met and changed. Experimental results, partly reported in the paper, confirm the method validity and also the robustness of the control under different pressure and temperature conditions. Some possible improvements have been enlightened in view of a full model-based controller.

6. Acknowledgments

The authors are grateful to anonymous reviewers for their useful remarks and suggestions. Part of the work of the authors from Politecnico di Torino has been supported by a grant from Atos SpA, Sesto Calende, Italy.

7. References

[1] D. Caputo "Digital motion control for position and force loops", *International Fluid Power Exposition and Technical Conference*, April 1996, paper I96-11.1.
[2] D. Halloran "Consider the advantages of digital hydraulic valves", *Hydraulics and pneumatics*, September 2002.
[3] L. Kelly and H-J. Haas "Hydraulic proportional valves with digital controllers", *International Fluid Power Exposition and Technical Conference*, April 1996, paper I96-11.5.
[4] C. Boes "The advantages of new proportional and servo valves with integrated digital electronics", *Moog Technical Papers*, 2003.
[5] Q.S. Lu, H. Bao and J. Li "Research on embedded electro-hydraulic proportional valve controller", *Proc. 2009 3rd IEEE Int. Symp. on Intelligent Information Technology Application*, pp. 91-94.
[6] E. Canuto "EmbeddedModel Control: outline of the theory", *ISA Transactions*, Vol. 46, No. 3, 2007, pp. 363-377.
[7] E. Canuto, W. Acuña-Bravo, A. Molano-Jimenez and C. Perez Montenegro "Embedded Model Control calls for disturbance modelling and rejection", *ISA Transactions*, Vol. 51 No. 5, 2012, pp. 584-595.
[8] E. Canuto, W. Acuna Bravo and C. Perez Montenegro "Robust control stability using the error loop", *Int. Journal of Mechatronics and Automation*, Vol. 3, No. 2, 2013, pp. 94-109.
[9] C. Kaddissi, J-P. Kenné and M. Saad, "Identification and real-time control of an electrohydraulic servo subsystem based on nonlinear backstepping", *IEEE/ASME Trans. on Mechatronics*, Vol. 12, No. 1, February 2007, pp. 12-22.
[10] Z. Sun and T.-W. Kuo, "Transient control of electro-hydraulic fully flexible engine valve actuation system", *IEEE Trans. on Control Systems Technology*, Vol. 18, No. 3, May 2010, pp. 613-621.
[11] D. Garagic and K. Srinivasan, "Application of nonlinear adaptive control techniques to an electro hydraulic velocity servomechanism", *IEEE Trans. on Control Systems Technology*, Vol. 12, No. 2, March 2004, pp. 303-314.
[12] Z. Sun and T.-C. Tsao, " Adaptive control with asymptotic tracking performance and its application to an electro-hydraulic servo system", *ASME J. Dyn. System, Meas. and Control*, Vol. 122, 2000, pp. 188-195.
[13] A. Mohanty and B. Yao, "Integrated direct/indirect adaptive robust control of hydraulic manipulators with valve deadband", ", *IEEE/ASME Trans. on Mechatronics*, Vol. 16, No. 4, August 2011, pp. 707-715.
[14] D.H. Kim and T.-C. Tsao "A linearized electrohydraulic servovalve model for vale dynamics sensitivity analysis and control system design", *ASME J. Dyn. System, Meas. and Control*, Vol. 122, 2000, pp. 179-187.
[15] E. Canuto, W. Acuna Bravo, M. Agostani and M. Bonadei, "Digital current regulator for proportional electro-hydraulic valves with unknown disturbance rejection", *ISA Transactions*, 2013, http:/dx.doi.org/j.isatra.2013.08.013.
[16] M. Agostani, M. Gamberoni, D. Butera and E. Canuto "Embedded model: application to electro-hydraulics",

Proc. of the 51st National Conference on Fluid Power, 2008, paper NCFP I08-5.5, pp. 141-145.

[17] E. Canuto E., F. Musso and L. Massotti "Embedded model control: application to electrovalves", *Proc.13th Mediterranean Conference on Control and Automation*, Limassol, Cyprus, June 27-29, 2005, pp. 952-957.

[18] E. Canuto and W. Acuna-Bravo "Hierarchical digital control of a proportional electro-hydraulic valve", *Proc. 2013 IEEE International Conference on Mechatronics and Automation,* August 4-7, 2013, Takamatsu, Japan, pp. 1015-1020.

[19] J. Ma, F. Wang, Z. Jia and W. Liu "Application of principal component analysis for mechanical coupling system modelling based on support vector machine", *Int. Journal of Mechatronics and Automation,* Vol. 1, No. 2, 2011, pp. 71-78.

[20] C. Mohtadi "Bode's integral theorem for discrete-time systems", *IEE Proceedings, Part D,* Vol. 137, No. 1999, pp. 57-66.

[21] J. S. Freudenberg and D. P. Looze "Right half-plane poles and zeros and design tradeoffs in feedback systems", *IEEE Trans. Automatic Control,* Vol. 30, No. 6, June 1985, pp. 555-565.

[22] C. Canudas de Wit, H. Olsson, K.J. Aström and A. Lischinsky "A new model for control of systems with friction", *IEEE Trans. Automatic Control*, 40, 1995, 419-425.

[23] S. Rosenbaum, M. Rudeman, T. Strohla and T. Bertram "Use of Jiles-Atherton and Preisach hysteresis models for inverse feed-forward control", *IEEE Trans. on Magnetics*, Vol. 46. No. 12, December 2010, pp. 3984-3989.

[24] J. Oh, B. Drincic and D.S. Bernstein "Nonlinear feedback models of hysteresis", *IEEE Control Systems Magazine,* February 2009, pp. 100-119.

[25] M.A.A. Shoukat Choudhurya, N.F. Thornhillb and S.L. Shaha "Modelling valve stiction", *Control Engineering Practice*, Vol. 13, 2005, pp. 641–658.

[26] A. Bonchis, P.I. Corke and D. C. Rye "Experimental evaluation of position control methods for hydraulic systems", *IEEE Trans. on Control Systems Technology,* Vol. 10, No. 6, 2002, pp. 876-882.